rf design studies on the 750 MHz radio frequency quadrupole linac for proton-induced x-ray emission analysis

Hermann Winrich Pommerenke,[1,2,*] Vittorio Bencini,[1] Alexej Grudiev,[1] Alessandra Maria Lombardi,[1] Serge Mathot,[1] Eric Montesinos,[1] Marc Timmins,[1] Ursula van Rienen,[2,3] and Maurizio Vretenar[1]

[1]*European Organization for Nuclear Research (CERN), CH-1211 Geneva 23, Switzerland*
[2]*Institute of General Electrical Engineering, University of Rostock, D-18051 Rostock, Germany*
[3]*Department Life, Light & Matter, University of Rostock, D-18051 Rostock, Germany*

(Received 29 March 2019; published 29 May 2019)

The proton-induced x-ray emission (PIXE) is the most commonly used ion beam analysis technique. It allows for nondestructive quantitative elemental characterization and is used in a variety of fields, particularly for the diagnosis of cultural heritage artwork. To provide mobile access to PIXE, a compact transportable radio frequency quadrupole (RFQ) linac has been designed and is being built at CERN. The PIXE RFQ has a length of only one meter and accelerates a proton beam to an energy of 2 MeV. This paper covers various rf design studies for the RFQ operating at 750 MHz. We show simulation results regarding cavity, equipment, and coupler geometry. Thermomechanical and beam dynamics studies are presented as well. The paper concludes with a conceptual study on dipole mode detuning by means of length adjustment.

DOI: 10.1103/PhysRevAccelBeams.22.052003

I. INTRODUCTION

In ion beam analysis, protons of a few MeV are used for material characterization, with the proton-induced x-ray emission (PIXE) [1] being the most widely used ion beam analysis technique. A 2 MeV to 4 MeV proton beam stimulates the emission of x-rays of specimen atoms. Measuring the spectrum allows for the quantitative and highly sensitive determination of elements in the material, with detection limits reaching ppm range. Due to its nondestructive character, PIXE is used in a variety of fields, for instance in atmospheric and environmental sciences, material sciences, quality control, and in particular the analysis of cultural heritage artwork.

Conventional electrostatic PIXE accelerators require significant space, infrastructure, and operating staff and are thus installed only in dedicated centers (e.g., [2–4]). However, due to a variety of reasons, for instance cost and feasibility, size, conservation stage, or immobility of, e.g., a fresco, it is often not acceptable to move the masterpiece to the facility. Contrarily, a compact high-frequency RFQ is able to provide 2 MeV protons over the length of just one meter. The PIXE RFQ [5,6] is developed and built at CERN within the context of the MACHINA project (Movable Accelerator for Cultural Heritage In situ Non-destructive Analysis, [7]), a collaboration between CERN and INFN. The aim of MACHINA is to build the first transportable system for *in situ* PIXE ion beam analysis, allowing employment in museums, restoration centers or even in the field.

The PIXE RFQ is a four-vane type structure designed and constructed with the experience gained from the Linac4 RFQ [8,9] and the high-frequency RFQ for medical applications (HF RFQ) [5,10–14]. It operates at a frequency of 749.48 MHz resulting in a small cavity with a cross section less than 14 cm wide [Figs. 1(b) and 1(d)]. Innovative beam dynamics have been developed to facilitate the 20 keV to 2 MeV acceleration over just one meter. Low power consumption has been an important optimization goal to allow for portability. The RFQ features a very short bunching section, entering at a synchronous phase of −30° which results in a comparatively low transmission of 30%. Also noteworthy are the average and minimum apertures of 1.439 mm and 0.706 mm, respectively. The constant vane tip radius of 1.439 mm significantly simplifies the machining as a rotating concave milling tool may be used. Table I lists a selection of the design parameters.

The PIXE RFQ is assembled from two half-meter modules. It features a total of 24 ports with a diameter of 36 mm that support the 16 tuners, seven pumping ports and the input power coupler, as well as eight additional smaller ports for rf field pick-up antennas. A CAD model is depicted in Fig. 1(a). Figure 1(c) shows the first module with openings where the equipment will be installed later.

*hermann.winrich.pommerenke@cern.ch

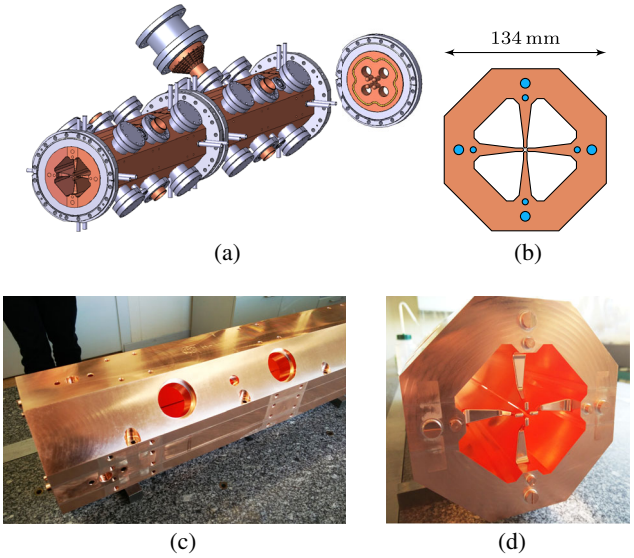

FIG. 1. CAD model of the PIXE RFQ linac with equipped tuners, pumping ports, coupler, and detached end plates with dipole stabilization rods (a) and cavity cross section with water cooling channels (b). Figures (c) and (d) show different views of the first module after the initial brazing.

This paper first focuses on the rf design studies conducted for the PIXE RFQ cavity, its particular end shapes and dipole stabilization rods, tuners, pumping ports, pick-up antennas, and the input power coupler. In Sec. II we summarize applicable constraints and approaches used to find the optimum geometry for each of these elements. Section III deals with the thermal behavior of the RFQ, which we study to estimate the mechanical deformation and resulting resonant frequency shift when the cavity is heated due to rf losses. In Sec. IV we present the beam dynamics simulations used to validate the rf design. We compare the results obtained from three different models and study the influence of the vane voltage. The effect of a detuned frequency on the beam dynamics is also evaluated concerning the expected shift from the thermal simulations. Lastly, Sec. V presents a conceptual study we conducted on dipole mode detuning by means of length adjustment instead of dedicated detuning geometries, which bears the potential for a significant increase in power efficiency.

TABLE I. Design parameters of the PIXE RFQ.

Input energy	$\mathcal{W}_{\mathrm{in}}$	20 keV
Output energy	$\mathcal{W}_{\mathrm{out}}$	2 MeV
rf frequency	f_0	749.48 MHz
Vane voltage	V_0	35 kV
RFQ length		1072.938 mm
Vane tip radius	ϱ_0	1.439 mm
Average aperture	r_0	1.439 mm
Minimum aperture	a	0.706 mm
Peak current		200 nA
Maximum duty cycle	d	2.5%
Repetition rate		200 Hz
Pulse duration		125 μs
Output beam diameter		0.5 mm
Transmission	T	30%
rf wall plug power		≤ 6 kVA

II. rf DESIGN

The rf design for the PIXE RFQ is initiated with a study on the 2D cross section, before 3D effects of the vane modulation are included. To achieve the desired spectral mode placement, end shapes with dipole rods are designed. Finally the geometries of tuners, pumping ports, pick-up antennas, and the input coupler are determined.

A. Cavity cross section

In general, all geometries are optimized to the resonant frequency $f_0 = \omega_0/2\pi$ while minimizing the surface power losses. This is expressed by a maximized quality factor $Q_0 = \omega_0 W/P_0$, where W is the stored energy and P_0 are the integrated losses over the entire interior surface.

While a circular shape of the four quadrants would be the optimum in this regard, the surfaces are chosen to be mostly planar to simplify machining [Figs. 1(b) and 2(b)]. For the same reason, the different cavity ports only intersect with one flat surface each, such that planar circular apertures are achieved. Additional constraints arise from the minimum material thickness between vacuum and water-guiding domains (≥4 mm) to avoid leakage, as well as mechanical stability and heat conductance considerations for the vanes. The resulting four quadrants have an almost triangular shape. The quality factor of this 2D computation is $Q_{0,2D} = 7280$.

Figure 2(a) shows the transverse electric field between the vane tips for the unmodulated case where the tips are at the average aperture of $r_0 = 1.439$ mm. The longitudinal magnetic field in the four quadrants is depicted in Fig. 2(b).

B. 3D effects of the vane modulation

The 3D shape of the modulated vanes deforms the electric field of the transverse electric (TE) mode to produce an accelerating component in the longitudinal direction. Consequently, the RFQ has to be considered as a tapered structure and 3D simulations are necessary.

To accurately represent the vane shape and its rf properties, a high mesh density is necessary. Figure 3 shows the mesh generated by ANSYS HFSS® [15] at the output end of the RFQ. An eigenmode computation based on the mechanical model, that due to symmetry conditions covers one quarter of the entire structure, requires roughly 1.2×10^6 tetrahedrons to converge; in total the simulation takes several days on a workstation machine (Intel Xeon CPUs, 24 Cores at 2.2 GHz, 500 GB RAM).

The modal capacitance between the vane tips depends on the local vane shape and is thus z-dependent. Each cell requires a slightly different cavity shape to tune the local

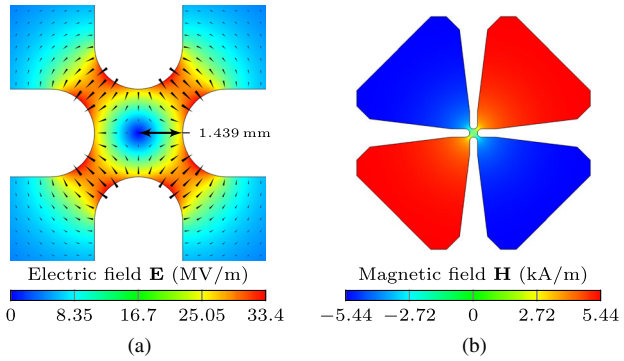

FIG. 2. Transverse electric field at the (unmodulated) vane tips (a) and longitudinal magnetic field in the RFQ cavities (b).

lumped LC circuit given by the vane capacitance and the cavity volume inductance. Since this is not feasible for machining, all geometric parameters of the cross section, except for the distance between the cavity back wall and the beam axis, are kept constant along the entire RFQ. The remaining degree of freedom is averaged over each of the two modules, such that apart from the vane tip only planar surfaces must be machined. For these fixed shapes, the capacitance, local resonance frequency and quality factor are shown in Fig. 4. Effectively detuning the local resonant circuit, the nonoptimum shape results in a nonuniform voltage distribution along the RFQ and must be compensated for by the tuners.

The 3D effects of the vane modulation, in particular curvatures of small radius and gaps, must also be considered when computing the maximum surface electric field. It is an important quantity as high fields may lead to electron emission and sparking. Computed using HFSS, the overall maximum of 39.1 MV/m occurs at the gap between the vanes of the two modules [Fig. 5(a)] due to the small rounding radius. This value corresponds to 1.55 Kilpatrick [16] at the given operating frequency. If this effect is ignored, the maximum field occurs in the bunching section of the RFQ [Fig. 5(b)] with 36.5 MV/m (1.44 Kilpatrick). This value agrees well with the prognosis of the PARMTEQ design tool [17] at 36.9 MV/m.

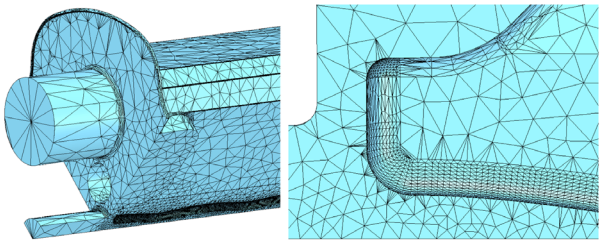

FIG. 3. Finite element mesh generated by HFSS at the output end (a) and close-up of the fine mesh used to represent the 3D-curved vane tips (b).

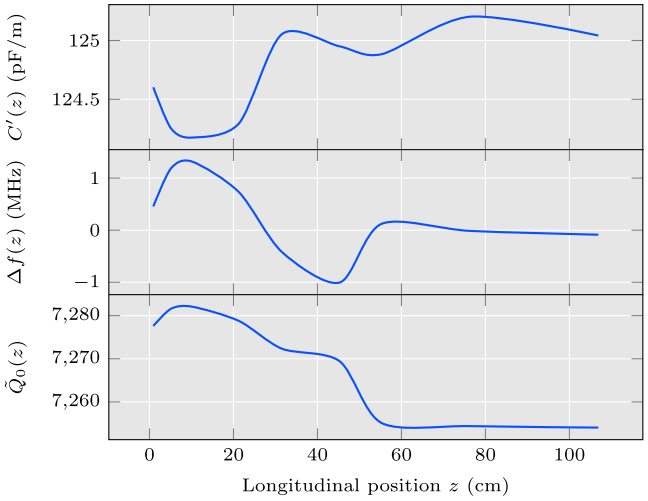

FIG. 4. Local modulation-dependent rf quantities. Capacitance over length, frequency offset and modulation-dependent quality factor are shown as functions of the longitudinal position. The second module is more homogeneous since it exclusively contains accelerating cells with high modulation depth.

C. End shapes and dipole stabilization rods

The capacitances between the vane noses and the end plates together with the inductances given by the vane undercuts, respectively, form resonant LC circuits. The nose shapes are effectively fixed by beam dynamics constraints. The undercuts are adjusted such that the lumped LC circuits act as open circuit boundary conditions on the operating quadrupole mode (TE_{210}). However, on all other modes they act as mismatched impedances inducing frequency shifts that cannot be neglected. To accurately represent these effects, 3D simulation tools or transmission line models have to be employed.

Small fabrication errors lead to mixing of modes of the ideal RFQ, which results in a perturbed field for the operating TE_{210} mode. The perturbation is proportional to the inverse of the squared frequency difference between

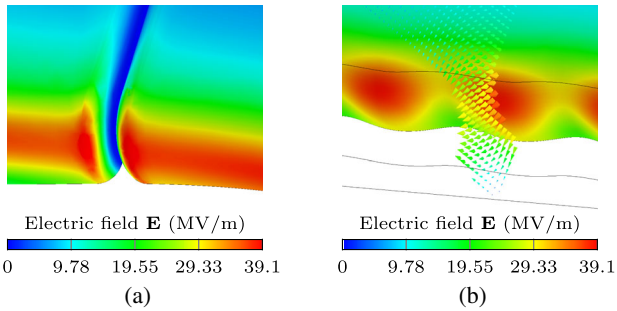

FIG. 5. Electric field on the modulated vane tip. The overall maximum occurs at the gap between the two RFQ modules with 39.1 MV/m (a). Neglecting the gap, the maximum is located in the bunching section with 36.5 MV/m (b). The plots use the same color scale for easier comparison.

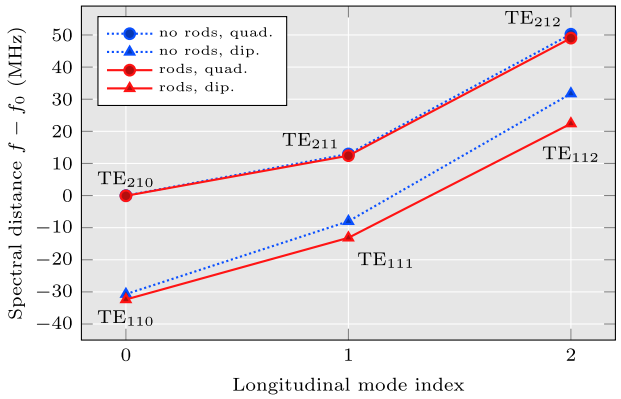

FIG. 6. Quadrupole and dipole mode spectrum of the PIXE RFQ without and with the employment of dipole stabilization rods.

the modes [18]. It is therefore desirable to have a maximum spectral separation between the operating mode and both lower and higher order modes. A common practice is the use of dipole stabilization rods (DSR) to tune the dipole mode frequencies away from the operating mode [10,19]. Due to the short length of the PIXE RFQ of 2.5λ the modes are initially quite well separated. We nevertheless used four DSRs on each end plate, each with a length of 2.5 cm, such that a mode separation of ± 12 MHz around the operating mode is achieved. The closest mode with a lower frequency is the second dipole mode (TE_{111}), and the neighbor with a higher frequency is the second quadrupole mode (TE_{211}). Figure 6 shows the effect of the DSRs on the PIXE RFQ spectrum.

The magnetic field at the output end and on the DSR is shown in Fig. 7. The surface current density is in magnitude equivalent to the tangential magnetic field. Its maximum of 25.1 kA/m is located at the edge of the vane undercut window.

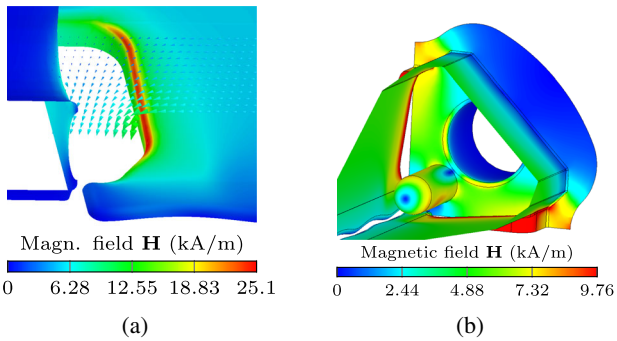

FIG. 7. Magnetic field (surface current density) at the output end. (a) Undercut window with the maximum tangential magnetic field throughout the entire RFQ at the undercut edge. (b) Field at the dipole stabilization rod. (Different color scales are used for clearer visualization).

D. Tuners, pumping ports, pick-up antennas

The PIXE RFQ features 16 tuners and seven vacuum pumping ports, which are assembled to a total of 24 flanges with an inner diameter of 36 mm. Four pumping ports are located in the first module, closer to the source and the regions of most expected particle losses. The input power coupler replaces one of the pumping ports in the second module. It is discussed further in Sec. II E.

The specific geometries are adapted from those of the HF RFQ for medical applications [5]. The tuners feature a conical tip to have a low impact on Q_0 while being convenient to manufacture. For the same reason, the pumping ports are designed with a single bar across the aperture providing a path for the surface currents. The penetration depth of the pumping ports into the cavity and the nominal tuner position are optimized to the operating frequency of the unperturbed cavity. Figure 8 shows the surface magnetic fields on the tips of tuner and pumping port.

The tuning setup is essentially the same as for the HF RFQ [5,12,13]. Four tuners each are installed at four longitudinal positions along the RFQ (1.6 tuners/λ per quadrant). The slugs have a movement range of ± 11 mm with respect to the nominal position, providing a frequency tuning range of approximatively ± 7.2 MHz.

Additional eight flanges for pick-up antennas are implemented. These antennas are simple magnetic loops connected to a coaxial transmission line. The designed antenna power is only 1 W, thus a very low coupling is required ($Q_{\mathrm{ext,Ant}} \approx 3.8 \times 10^8$). Figure 9 shows the magnetic field in the vicinity of the antenna.

E. Power loss and input coupler

The total rf power P_0 dissipated through surface losses may be accurately estimated without a full 3D simulation of the RFQ by longitudinally decomposing it into segments. The segments are chosen with respect to the components that imply a deviation from the ideal 2D geometry, such as tuners and pumping ports. By individual simulation, the

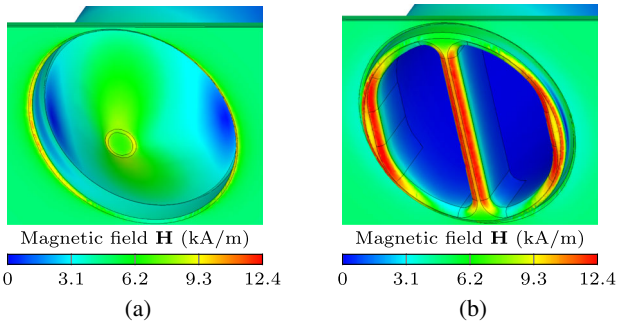

FIG. 8. Magnetic field at the tips of tuner and vacuum pumping port. The peak surface currents on the vacuum port are significantly higher, resulting in a larger impact on Q_0. (Identical color scales are used for easier comparison.)

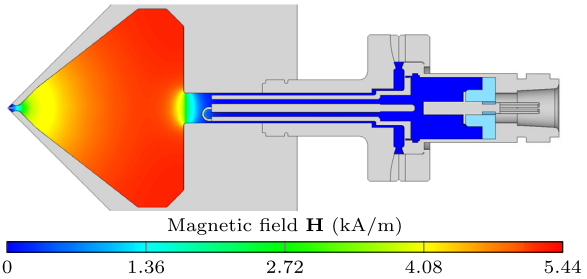

FIG. 9. Magnetic field at the pick-up antenna up to the ceramic rf window. The coupling is very low since the antenna is designed for a power of only 1 W.

quality factor $Q_{0,n}$ of each segment s is obtained. The capacitance over length $C'(z) = \mathrm{d}C/\mathrm{d}z$ changes along the accelerator due to the vane modulation and is interpolated by computing specific isolated cells (Fig. 4) to obtain the energy stored in the respective segment. Using $P_0 = \omega_0 W/Q_0$ and $W = CV_0^2/2$ for each segment we arrive at

$$P_0 = \omega_0 \frac{V_0^2}{2} \sum_{n=1}^{N} \frac{1}{Q_{0,n}} \int_{z_n}^{z_{n+1}} C'(z)\mathrm{d}z. \tag{1}$$

The quality factor $Q_{0,n}$ of the nth segment is obtained differently depending on the segment type. For the input and output end, it is computed directly by the respective 3D simulation. Otherwise it is obtained by integration over the interpolated quality factor profile $\tilde{Q}_0(z)$ (Fig. 4):

$$\frac{1}{\tilde{Q}_{0,n}} = \frac{1}{z_{n+1} - z_n} \int_{z_n}^{z_{n+1}} \frac{\mathrm{d}z}{\tilde{Q}_0(z)}. \tag{2}$$

Here, $\tilde{Q}_{0,n}$ solely considers the effect of the vane modulation, but not the influence of ports that may be present in that segment. For plain segments $Q_{0,n} = \tilde{Q}_{0,n}$, while the perturbation of tuners, pumping ports, or coupler in the port segments is accounted for by

$$Q_{0,n} = \tilde{Q}_{0,n} \frac{Q_{0,n}^{\mathrm{prt}}}{Q_{0,2\mathrm{D}}}, \tag{3}$$

where $Q_{0,n}^{\mathrm{prt}}$ is the quality factor of the nth segment with a port but no vane modulation. We assume that the relative change in quality factor due to the introduction of a port to a given plain, modulationfree segment n, i.e., the ratio $Q_{0,n}^{\mathrm{prt}}/Q_{0,2\mathrm{D}}$, is the same as if the segment contained modulated vanes, $Q_{0,n}/\tilde{Q}_{0,n}$. Equation (1) gives 64.1 kW for the nominal voltage $V_0 = 35$ kV, which is very close to the result of a full 3D simulation, 64.5 kW. The computed rf quantities are summarized in Table II.

The PIXE RFQ features one single input power coupler which replaces one of the vacuum pumping ports in the second module. It is a coaxial magnetic loop antenna.

TABLE II. Computed rf quantities for $V_0 = 35$ kV.

Quality factor	Q_0	5995
Capacitance	C'	125.1 pF/m
Stored energy	W	82.2 mJ
rf power loss	P_0	64.5 kW
Maximum surface field	E_s	39.1 MV/m

The coupler geometry is adapted from the HF RFQ design [10], which has been shown to be able transfer up to 100 kW [14]. The coupling loop has been enlarged and the overall penetration has been adjusted to account for the different cavity shape and higher coupling factor. The actual parameters are determined using the lumped RLC circuit model of the TE_{210} mode. The reflection coefficient is given by [20]

$$\Gamma = \frac{\beta - 1 - 2\mathrm{j}Q_0\Delta f/f_0}{\beta + 1 + 2\mathrm{j}Q_0\Delta f/f_0}, \tag{4}$$

where $\beta = Q_0/Q_{\mathrm{ext}}$ is the coupling coefficient and Δf denotes the offset between the natural resonance frequency of the cavity and the rf source frequency. The power loss P_0 in the walls of the cavity is implicitly fixed by the voltage and beam dynamics requirements; thus the required input power and reflected power are $P_{\mathrm{feed}} = P_0/(1 - |\Gamma|^2)$ and $P_{\mathrm{refl}} = P_0|\Gamma|^2/(1 - |\Gamma|^2)$, respectively.

Figure 10(a) shows a polar plot of the reflection coefficient. Critical coupling is achieved if $\beta = 1$ and $\Delta f = 0$. The marks denote operation points at 1% and 2.5% duty cycle, corresponding to cavity resonance shifts of 74.4 kHz and 186 kHz, that occur due to heat-induced deformation with the proposed cooling system. This is discussed in more detail in Sec. III. For the case of critical coupling, i.e., $\beta = 1$, the input impedance, reflection coefficient as well as input and reflected power are shown in Fig. 10(b) as functions of the frequency shift.

By design, the coupler is overcoupled at $\beta = 1.25$ as a safety margin accounting for deviations between simulated and real Q_0 factor. It is mounted on a rotatable flange to provide the possibility to adjust the coupling according to the measured Q_0, such that critical coupling is achieved after assembly.

Figure 11 shows the magnetic field in the vicinity of the coupler tip and in the coaxial waveguide at an rf phase of $\pi/2$, i.e., when the magnetic field in the RFQ quadrants reaches is peak value. Maxima occur at the edges of the holes for the bolts that attach the separately machined loop piece to the inner and outer conductors. The integrated power loss density and thus the effect on Q_0 are comparable to that of the vacuum pumping port.

The rf power is supplied via an EIA $3^{1/8}$ in 50 Ω coaxial waveguide filled with air. It is connected to the coupler by a taper and a polyether ether ketone (PEEK) vacuum window. Figure 12(a) shows the electric field

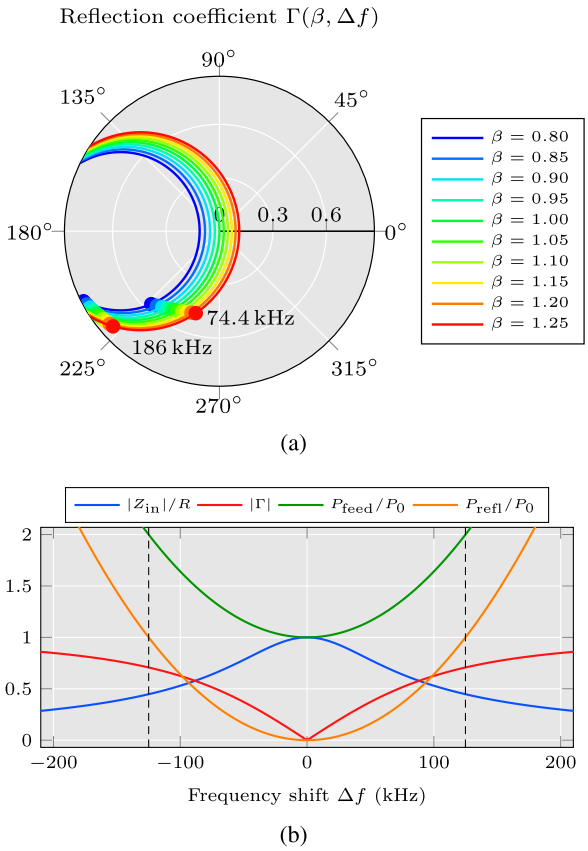

FIG. 10. A polar chart of the reflection coefficient depending on rf source frequency offset and coupling coefficient β is shown in (a). The points mark frequency shifts corresponding to a heat-induced deformation at operation with 1% and 2.5% duty cycle, respectively. For the case of $\beta = 1$ critical coupling, the input impedance, reflection coefficient, and powers are shown in (b) as functions of the frequency; the dashed lines mark the 3 dB bandwidth.

amplitude at the taper and the PEEK window when 65 kW are transmitted. Hotspots are located at the contact zones of the PEEK window and the coax inner conductor, as well as on the concave edge of the coupler

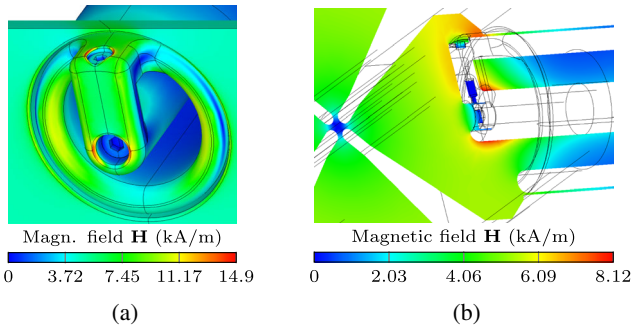

FIG. 11. Magnetic field at input power coupler at $\phi = \pi/2$ when the field has its maximum value. Hot spots are located on the edges of the bolt holes (a), while generally high currents are located on the edges of the loop and the border of the outer conductor (b).

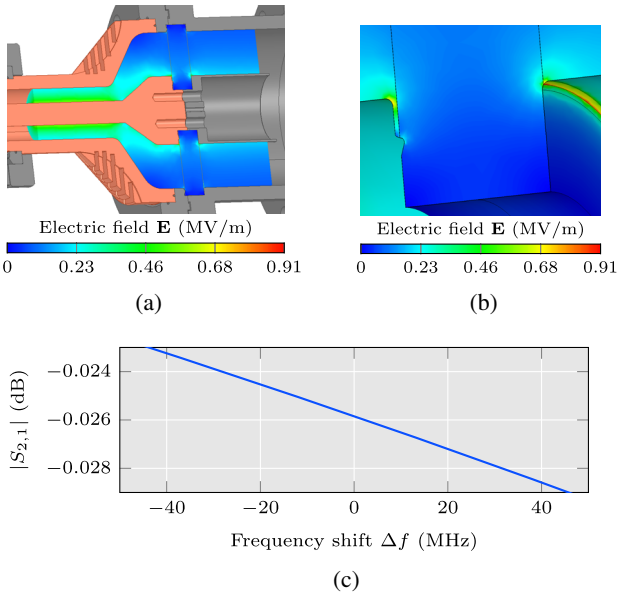

FIG. 12. Electric field amplitude at the taper and PEEK window of the input power coupler when 65 kW are transmitted (a). The maximum field of 0.91 MV/m is located at the contact of the PEEK window and the inner conductor of the coaxial waveguide (b). The transmission loss through PEEK window and taper is shown in (c).

inner conductor [Fig. 12(b)], with maximum values reaching 0.91 MV/m. Figure 12(c) shows the transmission $|S_{2,1}|$ through PEEK window and taper as a function of the frequency. At the operating frequency, the transmission loss is $|S_{21}| = -0.026$ dB.

III. THERMAL SIMULATIONS

During operation, the rf power is dissipated in the cavity walls, with a (peak) surface loss density $p_s = \Re\{Z_s H_t^2\}/2$ that acts as a heat source on the copper structure. Here, Z_s is the surface impedance and H_t denotes the tangential magnetic field. The heat is conducted away by eight water cooling channels per module. The resulting temperature increase and gradient causes a deformation of the copper and thus a detuning of the resonant frequency. We study the dependence of this effect on the duty cycle, cooling water temperature and flow speed with the help of the following tools: CST Microwave Studio® and Multiphysics Studio® [21], ANSYS HFSS® [15], ANSYS Mechanical® [22], and COMSOL Multiphysics® [23].

The heat transfer coefficients between bulk copper and cooling channel depend on the water flow speed: For 2 m/s, values of 7500 W/m^2/K and 7310 W/m^2/K are assumed for the 5 mm and 8 mm diameter cooling channels, respectively, while for 1 m/s both channels have 3900 W/m^2/K. Additionally, the copper-to-air convection is estimated with 10 W/m^2/K; it affects the thermal behavior insignificantly.

Figure 13 shows the distributions of surface losses, temperature, deformation and stress in 2D and 3D models for the operating point with $d = 2.5\%$ duty cycle, a cooling water temperature of $\vartheta_w = 22\,°C$ and a flow speed of $v_w = 1$ m/s. The average surface loss density $\langle p_s \rangle = d p_s$ is depicted in Fig. 13(a). Considering only the 2D cross section, the maximum temperature occurs in the vane tip with 3.7 K above the reference temperature of 22 °C [Fig. 13(b)]. This value is significantly exceeded (12.3 K above reference) when taking the 3D end shapes into account. The maximum temperature is located around the center of the end plate and the DSR, since they are only passively cooled via the flange connecting the end plate to the RFQ module [Fig. 13(d)]. The low duty cycle allows for a likewise passive cooling of the tuners, pumping ports, and input power coupler.

The frequency shift is dominated by two 2D effects illustrated by Fig. 13(c): the increasing tank size raises the volume inductance L of the cavity as the back wall moves by approximatively 3 μm. Due to the temperature gradient between the vanes and the tank, the vane tips move closer towards the beam axis (0.7 μm), increasing the capacitance C. This effect is only partially countered by the increasing tank size as it retracts the vanes from the beam axis. Both effects reduce the resonant frequency, since $\partial f/f = -(\partial C/C + \partial L/L)/2$ holds for the lumped LC circuit. The 3D deformation of the end shape effects the frequency detuning only marginally, however the occurrences of maximum stress are located here [Fig. 13(e)].

Within the considered parameter domain the frequency shift is linear with respect to duty cycle and water temperature, which is demonstrated in Fig. 14. The sensitivities are $\partial f/\partial \vartheta_w = -13.3$ kHz/K and $\partial f/\partial d = -74.4$ kHz/% for a 1 m/s water flow speed. The latter changes only slightly when doubling the water flow speed, however it would significantly increase the requirements on the chiller in the cooling circuit. Therefore, a flow speed of 1 m/s is chosen.

Since the 3 dB bandwidth of the PIXE RFQ cavity is only ±125 kHz, the frequencies of rf source and cavity have to match accurately to minimize the reflected power. Since no further accelerating structures are present, no frequency or phase stability is required at the output of the RFQ, and no frequency feedback loop to the cooling system is required. Instead, the rf power source follows the resonant frequency shift of the cavity. For the proposed range of operation of up to 2.5% duty cycle, the effect of the detuning on the beam dynamics is negligible, as is demonstrated in Fig. 19 of Sec. IV C.

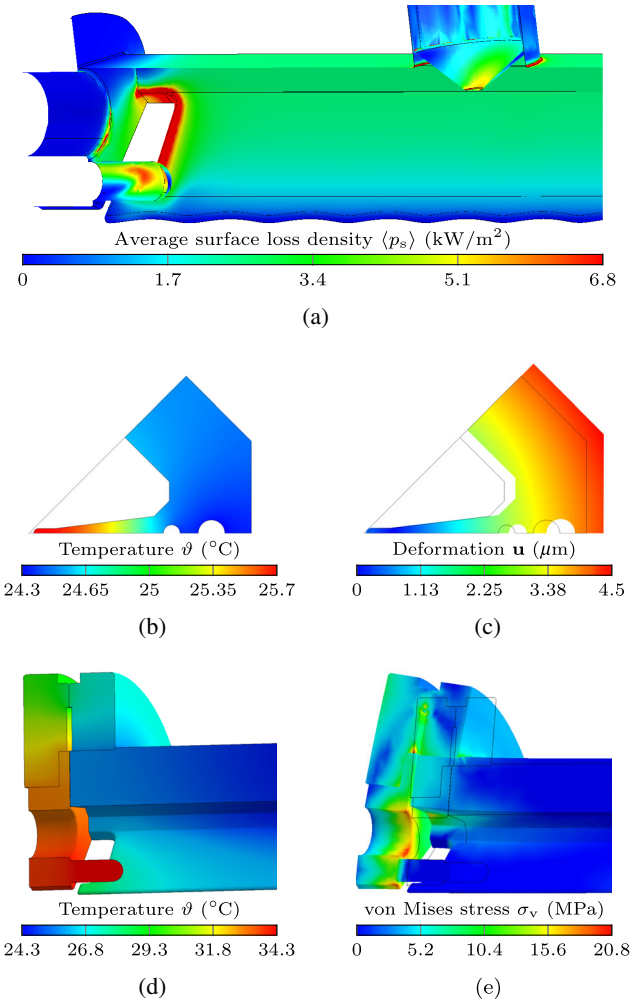

FIG. 13. Thermal simulation results for nominal operation parameters: duty cycle $d = 2.5\%$, water temperature $\vartheta_w = 22\,°C$, flow speed $v_w = 1$ m/s. Figure (a) shows the surface loss density on the output end, cavity wall and tuner tip (maximum value cut off for visualization purposes). The resulting temperature distribution is shown in (b) and (d). Figures (c) and (e) depict the corresponding deformation and equivalent stress.

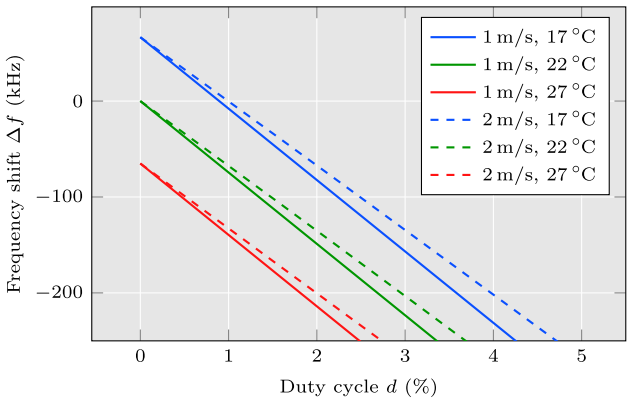

FIG. 14. Shift of the resonance frequency of the RFQ cavity subject to heat-induced deformation due to rf surface losses, with linear dependence on water temperature and flow velocity within the area of RFQ operation. The effect of reducing the water flow velocity is comparatively small.

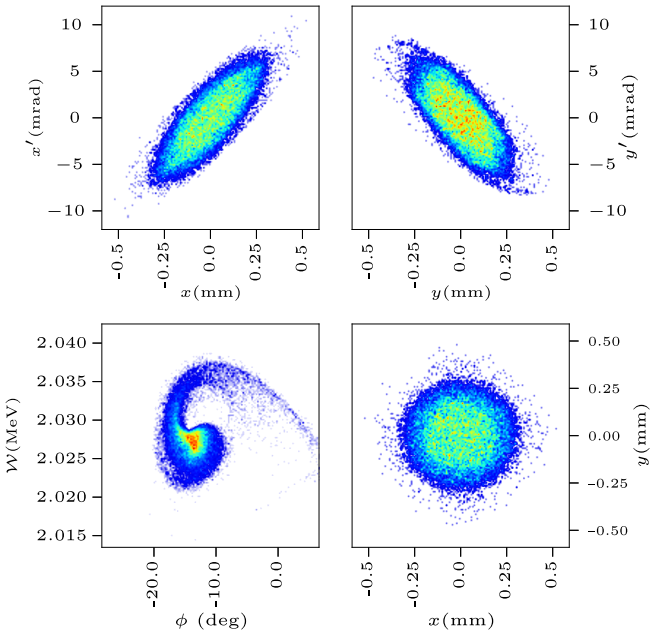

FIG. 15. Phase space at the output matching plane after tracking through the rf field simulated by HFSS for nominal operation parameters using TRAVEL. 29.0% of the dc input distribution are transmitted. The final energy of the bunch center is 2.028 MeV and the phase is −13.4°.

IV. BEAM DYNAMICS

The final rf design is validated by means of beam dynamics simulations, where a distribution of macroparticles is tracked through the electromagnetic field while it is subject to Lorentz force and potentially space charge forces. For constant-voltage RFQs the magnetic field is practically zero in vicinity of the beam axis, such that only forces caused by the electric field need to be considered. In the special case of the PIXE RFQ, the space charge forces are also negligibly small due to the low beam current of 200 nA at the output plane, which simplifies the particle tracking simulation.

A. Model comparison

Figure 15 shows the 6D phase space at the output matching plane if an unbunched beam is applied at the input matching plane. This distribution is obtained when tracking through the field map produced by HFSS at nominal parameters (Table I) using TRAVEL [24]. Virtually identical results can be produced by using TRACEWIN [25]. The transmission T is defined as the fraction of particles that are accelerated and reach the output plane; it reads $T = 29.0\%$ for the HFSS field map. The final average energy is $\mathcal{W}_{\mathrm{out}} = 2.028$ MeV and the final synchronous phase is $\phi_s = -13.4°$.

We compare these results to the output distribution produced by the tracking tool that is part of the PARMTEQ RFQ design tool chain [17]. It relies on an analytic potential representation using the eight lowest-order terms of a multipole expansion (eight-term potential function) [18,26], which is valid for the electric field between the vane tips. The expansion coefficients are obtained from lookup tables that have been precomputed for different vane geometries [26].

Additionally we draw a comparison to the previously mentioned models by simulating the particle trajectories through a field map generated from the eight-term potential function using TRAVEL. Here, the multipole expansion coefficients are identical to those used by PARMTEQ.

In general, a very good agreement between the phase spaces generated by PARMTEQ, as well as by tracking through the reproduced eight-term potential field map and HFSS field map, is observed. The transverse planes are virtually identical, but differences are visible in the longitudinal plane (Fig. 15, lower left). The phase spaces of PARMTEQ and the eight-term potential are depicted in Figs. 16(a) and 16(b), respectively. Their macroscopic shapes agree very well compared to the more twisted form of the HFSS field (Fig. 15, lower left). However, the final energy of the PARMTEQ result is lower and the transmission is higher compared to the other two models. A selection of the phase space parameters is presented in Table III.

The observed differences between the models may partially be explained by the different algorithms used by the codes TRAVEL and PARMTEQ, particularly their particle loss models. While TRAVEL is a general purpose tracking tool using an rf field map, PARMTEQ is tailored to the characteristics of RFQ and makes certain simplifications. For details we refer to [17,24]. It should also be noted that the differences are small ($\lesssim 1\%$), such that while they are clearly visible in simulation, they will likely not be measurable in the real RFQ setup.

Instead of the phase spaces, one may also examine the multipole expansion coefficients to validate the rf field. Figure 17 shows the eight coefficients of the eight-term potential computed from the HFSS field map as functions of the longitudinal cell position (solid lines). The respective

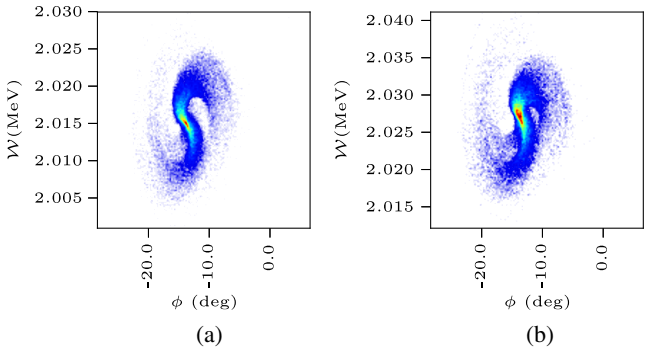

FIG. 16. Longitudinal phase spaces at the output matching plane produced by PARMTEQ (a) and after tracking through a field map generated from the same eight-term potential function using TRAVEL (b).

TABLE III. Output phase space parameters.

		PARMTEQ	8-term potential	HFSS field
Transmission	T	32.44	29.34	29.02%
Energy	$\mathcal{W}_{\text{out}}$	2.015	2.027	2.028 MeV
rms energy spread	$\sigma_{\mathcal{W}}$	4.0	3.7	3.3 keV
Synchronous phase	ϕ_s	−14.7	−17.2	−13.4°
Horizontal rms emittance	$\varepsilon_{xx'}$	0.0170	0.0169	0.0166 π mm mrad
Vertical rms emittance	$\varepsilon_{yy'}$	0.0173	0.0169	0.0169 π mm mrad
Transverse rms emittance	ε_{xy}	0.0178	0.0179	0.0179 π mm^2
Longitudinal rms emittance	$\varepsilon_{\phi\mathcal{W}}$	0.0088	0.0086	0.0124 π MeV

values obtained from the PARMTEQ design tool chain [17] serve as references (dotted lines). Some of them are multiplied by their accompanying modified Bessel function $\mathcal{I}(\cdot)$ for visualization purposes. Of special interest are the quadrupole focussing strength $A_{0,1}$ and the acceleration efficiency $A_{1,0}$. Apart from numerical noise, the agreement is very good with an error less than 1%. The nevertheless noticable differences could originate from the tapering of the vane tips, which is required to obtain a smooth continuous surface but neglected by the eight-term potential function representation. The gap between the two RFQ modules [shown in Fig. 5(a)] is observed to have a particular effect on the multipole components with quadrupolar field patterns, and is visible as a small dent in the respective $A_{0,1}$ and $A_{2,1}$ lines.

B. Dependence on vane voltage

The differences between the three models are also visible in Fig. 18, which shows the transmission, final energy, and final synchronous phase in dependence of the vane voltage V_0. The curves show a threshold behavior originating in the gentle buncher, where a minimum voltage is required to form the bucket and capture the particles from the unbunched input beam. For both models that rely on the potential function it is located at roughly 33.7 kV, while for the HFSS field the value reads approximatively 34.4 kV. In the stable region, the tracking results of the eight-term potential and HFSS field maps show very good agreement.

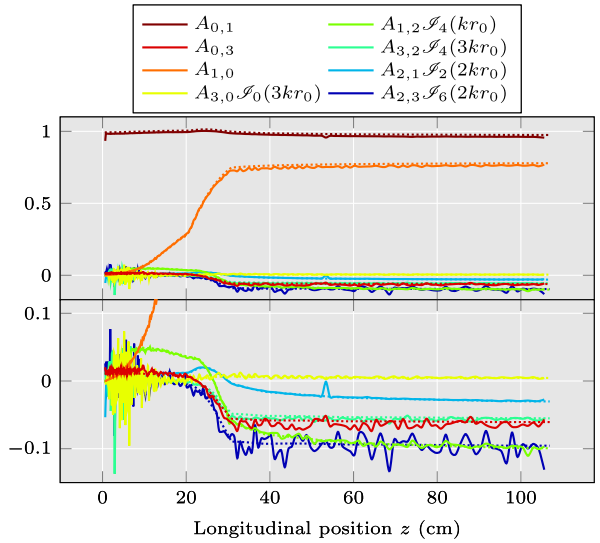

FIG. 17. Comparison between the eight multipole expansion coefficients computed from the HFSS field (solid) and their design values (dotted) for each RFQ cell. The bottom plot enlarges a region of the upper graphic to enhance the visualization of the higher order terms.

C. Dependence on frequency

Lastly, we study the influence of the rf frequency on the beam dynamics. This is of special interest in conjunction with the thermal simulations performed in Sec. III: Fig. 19 demonstrates that the dependence of transmission and final energy on the frequency are approximatively linear. An increase in frequency means the particle arrives later in each cell and thus closer to the crest ($\phi = 0$) of the electric field oscillation. This results in a decrease of the longitudinal phase acceptance, lowering the transmission, and in

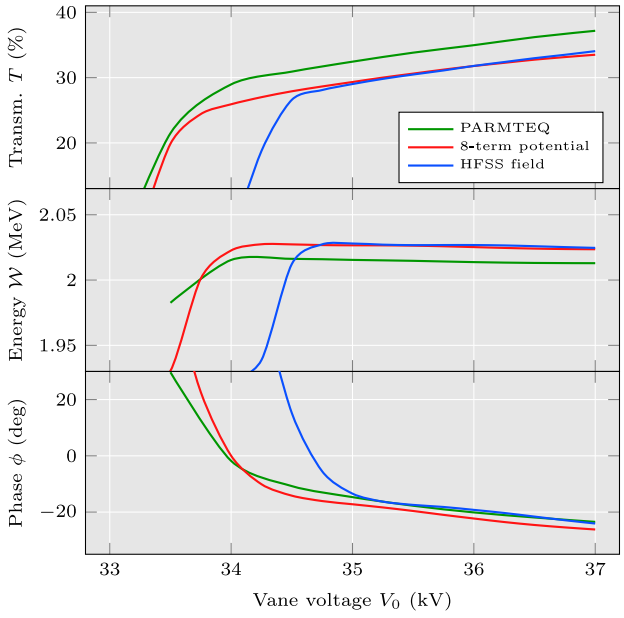

FIG. 18. Transmission, final energy, and final synchronous phase as functions of the vane voltage for the three investigated field models.

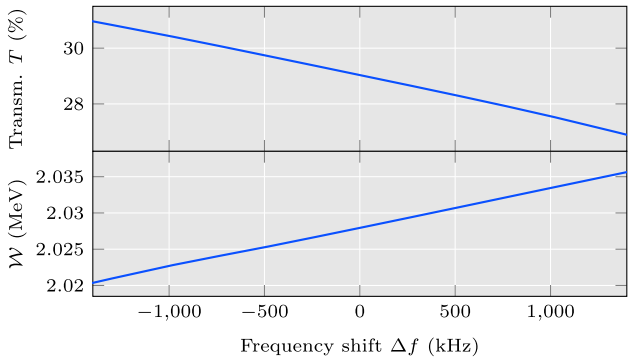

FIG. 19. Transmission and final energy as functions of the rf frequency. The magnitude of the frequency shift caused by the heat-induced deformation of the cavity is expected to be less than 200 kHz.

an increase of the integral electric field seen by the particle, increasing the final energy. The effect of a heat-induced detuning of −186 kHz corresponding to 2.5% duty cycle is negligibly small.

V. DIPOLE MODE DETUNING BY LENGTH ADJUSTMENT

A conceptual study has been performed on the dipole mode detuning by means of RFQ length adjustment. Generally, the length is fixed by the beam dynamics design, and lower or higher order modes are detuned by means of DSRs, among others, as it has been accomplished for the PIXE RFQ (see Sec. II C and Fig. 6). Disadvantages of these DSRs are that they introduce additional power losses and complicate the fabrication process.

The RFQ acts like a dispersive transmission line [18] with longitudinally varying circuit elements, since it is effectively a tapered waveguide due to the vane modulation. For instance, the capacitance of the quadrupole mode is shown in Fig. 4. The ends act as additional impedances terminating the transmission line, and are mismatched for all but the TE_{210} operating mode. Such models have been used to describe and tune the spectra of RFQs, e.g., in [9,19,27,28] to name a few.

As an alternative to DSRs, one can estimate the required length for a specific mode placement from the mentioned transmission line model. Appending additional accelerating cells at the end of the RFQ gives the desired spectrum, which can be verified by means of rf simulations. Figure 20

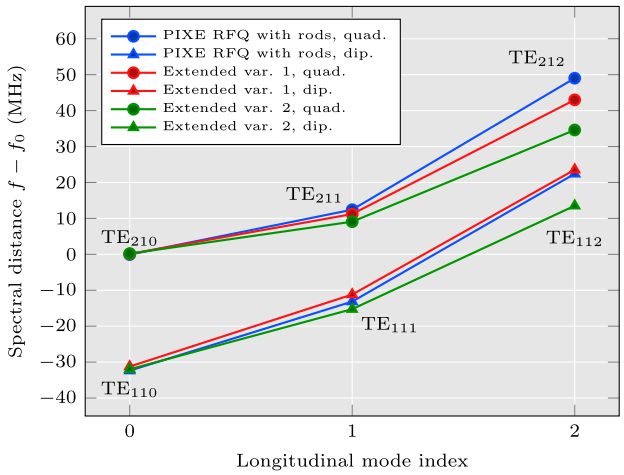

FIG. 20. Spectrum of PIXE RFQ with dipole stabilization rods compared to the spectra obtained by omitting the rods and extending the length of the cavity.

depicts the spectra of two variants obtained from extending the PIXE RFQ. Variant 1 achieves roughly the same spectral margins as the PIXE RFQ with rods (which is also shown) using seven additional cells (≈10 cm, +10%) and waiving DSRs. The modes TE_{111} and TE_{211} are almost symmetrically arranged around the operating mode. Variant 2 extents the PIXE RFQ by 17 cells (≈24 cm, +23%) to achieve the largest possible distance to the closest dipole modes TE_{111} and TE_{112} while accepting a closer higher order quadrupole mode (TE_{211}). A significant difference compared to the use of DSRs is that the latter (in a very good approximation) only affects the dipole modes, while a change in length detunes all modes apart from the lowest order quadrupole and dipole modes resonating at cut off frequency.

The addition of accelerating cells obviously leads to an increase in output energy, but also to an increase in power consumption due to the additional surface area. However, the overall quality factor Q_0 is higher since the DSRs are not present. The higher output energy bears the potential to lower the vane voltage, which would significantly lower the power consumption ($P_0 \propto V_0^2$). Table IV shows theoretical estimates for the power savings potential by reducing the voltage, if the same output energy is achieved over a longer accelerator. However, the thereby inevitable adjustment to the beam dynamics and the vane modulation changes the modal capacitances and thus again the spectrum.

TABLE IV. Estimation of extended RFQ power loss.

	Length	Q_0	Voltage	Output energy	Power
PIXE RFQ with rods	107 cm	5995	35 kV	2.03 MeV	65 kW
Extended variant 1	117 cm	6230	35 kV	2.17 MeV	67 kW
Extended variant 2	131 cm	6310	35 kV	2.41 MeV	74 kW
Variant 1 reduced V_0	117 cm	(6230)	33 kV	2.03 MeV	(60 kW)
Variant 2 reduced V_0	131 cm	(6310)	30 kV	2.03 MeV	(55 kW)

(The parentheses in the table emphasize that this is neglected in the initial estimation.) This leads to an iterative procedure of successive beam dynamics studies and eigenmode computation, which we expect to converge within a few iterations. With the aim of a fast design procedure, it is advantageous to rely on semianalytical models, i.e., the eight-term potential function for the beam dynamics and the transmission line model for the eigenmodes, that have been proven to be reliable. The computationally far more costly rf simulations should be performed at the end of the design study as a mean of validation. This novel approach will be used in the design of future RFQs.

VI. CONCLUSION

The rf design of the PIXE RFQ has been completed and geometrical dimensions for cavity, ends and dipole rods, tuners, vacuum pumping ports, pick-up antennas and input power coupler have been determined for the mechanical design and machining.

The thermomechanical behavior of the structure has been studied to anticipate temperature distribution and deformation as well as the shift on the resonant frequency for nominal operation parameters. A cost-efficient cooling system without frequency feedback will be used resulting in an RFQ resonant frequency shift that is linear with respect to its duty cycle. In order to minimize the power reflected from the RFQ cavity, the rf power source has to follow this shift.

Beam dynamics simulations show that the frequency shift is acceptable. In this context, we have also drawn a comparison between the predicted phase space obtained from the RFQ design tools to the distribution obtained from tracking through the rf field map. Good agreement has been observed and the rf design has been validated.

Lastly, we have presented an initial study on dipole mode detuning by means of length adjustment. The absence of dipole rods increases the quality factor and simplifies the fabrication, while a possible voltage reduction due to the gained length would reduce the overall power consumption. This subject requires further studies that will likely lead to an iterative procedure to determine the final shape of the RFQ.

ACKNOWLEDGMENTS

This work has been supported by the CERN Knowledge Transfer Group and the PhD Project leading to this article is sponsored by the Wolfgang Gentner Programme of the German Federal Ministry for Education and Research (BMBF, Grant No. 05E15CHA).

[1] S. A. E. Johansson, J. L. Campbell, K. G. Malmqvist, J. D. Winefordner *et al.*, *Particle-Induced X-ray Emission Spectrometry (PIXE)* (John Wiley & Sons, New York, 1995), Vol. 133.

[2] P. A. Mandò, M. E. Fedi, N. Grassi, and A. Migliori, Differential PIXE for investigating the layer structure of paintings, Nucl. Instrum. Methods Phys. Res., Sect. B **239**, 71 (2005).

[3] S. Limandri, C. Olivares, L. Rodriguez, G. Bernardi, and S. Suárez, PIXE facility at Centro Atómico Bariloche, Nucl. Instrum. Methods Phys. Res., Sect. B **318**, 47 (2014).

[4] M. Vadrucci, G. Bazzano, F. Borgognoni, M. Chiari, A. Mazzinghi, L. Picardi, C. Ronsivalle, C. Ruberto, and F. Taccetti, A new small-footprint external-beam PIXE facility for cultural heritage applications using pulsed proton beams, Nucl. Instrum. Methods Phys. Res., Sect. B **406**, 314 (2017).

[5] M. Vretenar, E. Montesinos, M. Timmins, M. Garlaschè, A. Grudiev, S. Mathot, B. Koubek, V. Dimov, A. M. Lombardi, and D. Mazur, High-frequency compact RFQs for medical and industrial applications, in *Proceedings of the 28th Linear Accelerator Conference (LINAC2016)* (JACoW, Geneva, Switzerland, 2016), pp. 704–709.

[6] H. W. Pommerenke, A. Bilton, A. Grudiev, A. M. Lombardi, S. Mathot, E. Montesinos, M. Timmins, M. Vretenar, and U. van Rienen, rf design of a high-frequency RFQ linac for PIXE analysis, in *Proceedings of the 29th Linear Accelerator Conference (LINAC2018)* (JACoW, Geneva, Switzerland, 2018), pp. 822–825.

[7] L. Giuntini, G. Anelli, S. Atieh, A. Bilton, L. Castelli, G. Calzolai, M. Chiari, C. Czelusniak, M. E. Fedi, A. Grudiev, A. M. Lombardi, M. Manetti, S. Mathot, E. Montesinos, L. Palla, F. Taccetti, M. Timmins, and M. Vretenar, MACHINA: Movable accelerator for cultural heritage in-situ non-destructive analysis, in *Proceedings of the 16th International Conference on Nuclear Microprobe Technology and Applications (ICNMTA2018)* (2018) (to be published).

[8] S. Mathot, P. Bourquin, A. Briswalter, T. Callamand, J. Carosone, N. Favre, J. M. Geisser, A. M. Lombardi, V. Maire, M. Malabaila, D. Pugnat, P. Richerot, B. Riffaut, C. Rossi, M. Timmins, A. Vacca, G. Vandoni, and M. Vretenar, Mechanical design, brazing and assembly procedures of the Linac4 RFQ, in *Proceedings of the International Particle Accelerator Conference, Kyoto, Japan* (ICR, Kyoto, 2010), pp. 807–809.

[9] O. Piquet, O. Delferrière, M. Desmons, A. C. France, A. M. Lombardi, C. Rossi, and M. Vretenar, The rf design of the linac4 RFQ, in *Proceedings of the International Particle Accelerator Conference, Kyoto, Japan* (ICR, Kyoto, 2010), pp. 738–740.

[10] M. Vretenar, A. Dallocchio, V. A. Dimov, M. Garlaschè, A. Grudiev, A. M. Lombardi, S. Mathot, E. Montesinos, and M. Timmins, A compact high-frequency RFQ for medical applications, in *Proceedings of the 27th Linear Accelerator Conference (LINAC2014)* (JACoW, Geneva, Switzerland, 2014), pp. 935–938.

[11] A. M. Lombardi, E. Montesinos, M. Timmins, M. Garlaschè, A. Grudiev, S. Mathot, V. Dimov, S. Myers, and M. Vretenar, Beam dynamics in a high-frequency RFQ, in *Proceedings of the 6th International Particle Accelerator Conference (IPAC2015)* (JACoW, Geneva, Switzerland, 2015), pp. 2408–2412.

[12] B. Koubek, Y. Cuvet, A. Grudiev, C. Rossi, and M. Timmins, Tuning of the CERN 750 MHz RFQ for medical applications, in *Proceedings of the 28th Linear Accelerator Conference (LINAC2016)* (JACoW, Geneva, Switzerland, 2016), pp. 763–766.
[13] B. Koubek, A. Grudiev, and M. Timmins, rf measurements and tuning of the 750 MHz radio frequency quadrupole, Phys. Rev. Accel. Beams **20**, 080102 (2017).
[14] V. A. Dimov, M. Caldara, A. Degiovanni, L. S. Esposito, D. A. Fink, M. Giunta, A. Jeff, A. Valloni, A. M. Lombardi, S. J. Mathot, and M. Vretenar, Beam commissioning of the 750 MHz proton RFQ for the LIGHT prototype, in *Proceedings of the 9th International Particle Accelerator Conference (IPAC2018)* (JACoW, Geneva, Switzerland, 2018), pp. 658–660.
[15] ANSYS, Electromagnetics Suite, release 18.2, (2017).
[16] W. D. Kilpatrick, Criterion for vacuum sparking designed to include both rf and dc, Rev. Sci. Instrum. **28**, 824 (1957).
[17] K. R. Crandall and T. P. Wangler, PARMTEQ—a beam dynamics code for the RFQ linear accelerator, AIP Conf. Proc. **177**, 22 (1988).
[18] T. P. Wangler, *RF Linear Accelerators*, 2nd ed. (John Wiley & Sons, 2008).
[19] F. Grespan, A. Pisent, and A. Palmieri, Dipole stabilizers for a four-vane high current RFQ: Theoretical analysis and experimental results on a real-scale model, Nucl. Instrum. Methods Phys. Res., Sect. A **582**, 303 (2007).
[20] R. E. Collin, *Foundations for Microwave Engineering*, 2nd ed. (McGraw-Hill, New York, 1992).
[21] Computer Simulation Technology, CST Studio Suite, release 2018, (2018).
[22] ANSYS, Mechanical, release 18.2, (2017).
[23] COMSOL, COMSOL Multiphysics, version 5.3a, (2017).
[24] A. Perrin, J.-F. Amand, T. Mütze, and J.-B. Lallement, *Travel v4.07 User Manual* (CERN, Geneva, 2017).
[25] D. Uriot and N. Pichoff, *TraceWin Documentation* (CEA, Saclay, 2011).
[26] K. R. Crandall, Effects of vane tip geometry on the electric fields in radio frequency quadrupole linacs, Los Alamos National Laboratory Technical Report No. LA-9695-MS, 1983, https://inspirehep.net/record/190458.
[27] A. Simoens, A. France, and O. Delferrière, An equivalent 4-wire line theoretical model of real RFQ based on the spectral differential theory, in *Proceedings of the 21st International Linac Conference, Gyeongju, Korea, 2002* (Pohang Accelerator Laboratory, Pohang, Korea, 2002).
[28] A. Palmieri, F. Grespan, and A. Pisent, Perturbation analysis on a four-vane RFQ, in *Proceedings of the International Particle Accelerator Conference, Kyoto, Japan* (ICR, Kyoto, 2010), pp. 606–608.